Electronic Supplementary Material (ESI) for Journal of Materials Chemistry A.

Supplementary Information

Oppositely Charged MXene Fibers as Highly Efficient Osmotic Power Generator from Sea and River Water

Fatemeh Hashemifar, Ali Esfandiar*

Department of Physics, Sharif University of Technology, Tehran 11155-9161, Iran.

**Corresponding authors: esfandiar@sharif.edu*

Keywords: MXene membrane fiber, Nanofluidics, Ion selectivity, Nanoconfined fluidic channels, Osmotic energy harvesting

Supplementary Notes

Note S1. Synthesis of the negatively and positively MXene

The negatively charged $Ti_3C_2T_x$ MXene was synthesized from Ti_3AlC_2 MAX phase by selectively etching Al atomic layers as follows MILD method. All chemical materials were purchased from Sigma-Aldrich and were used as received. By dissolving 1.6g LiF in 20mL of 9M HCl, the etching solution was obtained. In the next step, 1g Ti_3AlC_2 powder was slowly added to the solution with magnetic stirring for 40 hours at 35℃. The resulting reaction was washed with deionized water until self-delamination occurred and the pH of supernatant 6. In synthesis, $Ti_3C_2T_x$ is obtained by following these equilibria[1]:

$$Ti_3AlC_2 + 3LiF + 3HCl \leftrightarrow Ti_3C_2 + AlF_3 + 3LiCl + 3/2\ H_2 \quad (S1)$$

$$Ti_3C_2 + 2\ H_2O \leftrightarrow Ti_3C_2(OH)_2 + H_2 \quad (S2)$$

$$Ti_3C_2 + H_2O \leftrightarrow Ti_3C_2O + H_2 \quad (S3)$$

$$Ti_3C_2 + 2HF \leftrightarrow Ti_3C_2F_2 + H_2 \quad (S4)$$

Then, the dispersion was centrifuged at 3500 rpm for 1 hour to remove unexfolited MXene. The positively charged MXene flakes were prepared by the dropwise addition of the polydiallyl dimethyl ammonium chloride (PDDA) solution (2.5 mL, 20w% aqueous solution) into the colloidal solution of the negatively MXene (120mL; 0.4mg mL^{-1})[2]. The mixture was magnetically stirred at room temperature for 24 hours. Then the solution was washed with deionized water and centrifuged two times at 3500 rpm for 1 hour. Finally, the positively charged MXene flakes were obtained by redispersing sediment into DI water.

Note S2. The wet spinning of N-MF and P-MF

Aqueous negatively (30 mg mL^{-1}) and positively (24 mg mL^{-1}) MXene were readied and loaded into a syringe with a spinning nozzle (gauge 25) and injected into a rotating Petri dish containing

the coagulation bath, which was placed into an ice-water bath (Fig. 2f). An injection pump (Top-5300) was used to handle the spinning rate which was 23 mLh^{-1} for N-MF and 12 mLh^{-1} for P-MF. Fiber streching during coagulation causes a well-aligned structure in the fiber [3]. Consequently, using the low velocity of wet spinning can result in high drawing and orientation. On other hand, the MXene solution gets clogged when extruding through the nozzle, and we have to use high-velocity of wet spinning to prevent clogging. Therefore, we used the lowest spinning rate that did not block the needle and allowed us to produce continuous fiber.

The coagulation aqueous solution was a mixture of isopropanol (IPA, a poor solvent for solidifying MXene sheets) and DI water (with relatively higher density to defy the gravitational effects of gel fibers) (IPA to water volume rate at 9/1) with 5w% $CaCl_2$ (for coulombic force interlinking among flakes) (Fig. S6). After 30 minutes, gel-state MXene fibers were rinsed and dried naturally for about 1 hour at room temperature.

Note S3. Characterization of MXene flakes and fibers

MAX and MXene powder and wet spun fibers were characterized with an X-ray diffractometer (Xpert MPD) using a Cu k-Alpha radiation source ($\lambda = 1.54$ Å) (Fig. 2h and Fig. S1). The surface morphologies of the MXene nanosheets were studied via atomic force microscopy (AFM) (Park Scientific CP-Research, VEECO) in tapping mode (Fig. S2). Using the dynamic light scattering (DLS, Malvern) technique from an average of five measurements, the size distribution of MXene sheets in dispersions was evaluated (Fig. S3). The SEM images were obtained using a T-scan MIRA3 system operating at 5 KeV (Fig. 2i, 2j, 3g, S4, S7, S9, and S11). The surface chemical groups of N-MX and P-MX were characterized by Fourier transform infrared spectroscopy (FTIR, Bruker) in the wavenumber range of 400-4000 cm^{-1} (Fig. 2c). Using nanometer particle size and zeta potential analyzer, the zeta potentials of N-MX and P-MX were measured (Fig .2d). The liquid crystal texture of MXene flakes was observed by Zeiss Axio Scope in polarized optical microscopy mode (Fig. S5).

Note S4. Chemical Stability of MXene Fibers

To investigate chemical stability in the solutions and the fixed size of the nanochannels, we embedded MXene fibers in saline solution for two months and performed analyzes to compare fresh fiber and salt solution-immersed fiber.

Due to the electrochemical stability and electrostatic attraction between the MXene sheets and ions, the fibers sustain from disintegration in water. As shown in Fig. S10, we did not observe any integration and instability of MXene fibers after two months of immersion in water and saline. Furthermore, the oxidation of MXene fibers in an aqueous solution was tested. Comparing oxygen in Fig. S11 observe that there is no significant change in the amount of oxygen in fresh fiber and fiber after immersed in saline solution.

Note S5. Ion transport measurements

The plexiglass plates, which contain epoxy encapsulated MXene fibers, were placed between two reservoirs (with a capacity of 3mL each) (Fig. 3a) and then made a leak-tight environment sealed by using O-rings from both sides. Ion conductivity was tested between the two reservoirs with the same concentration, ion selectivity was measured with a salinity concentration gradient from 10-1000 folds between two reservoirs, and the NP-MF cell was investigated with the adjacent N-MF, and P-MF formed three reservoirs which were filled from artificial river water (0.01 M NaCl) and seawater (0.5 M NaCl), through cycle voltammetry (CV) in the potential range of -0.2V to +0.2V with the step voltage of 0.01V. In addition, Ag/AgCl electrodes were utilized to exert a transmembrane potential across the membrane and record the current-voltage response. The ion transport properties of the individual P-MF and N-MF membranes were measured by ZAHNER (IM6ex) instrument. The pH was adjusted using HCl and KOH solutions and measured with a pH meter (Metrohm).

Note S6. Effect of coagulation bath temperature on wet spinning

A decrease in bath temperature can reduce the double-diffusion driving force between the solvent (water) and non-solvent (IPA) in the coagulation process, so water molecules have more

time to leave the gel structure before coagulating the surface of the fiber, which leads to a densely packed formatting in the fiber [4,5]. We performed the wet spinning process at different coagulation temperatures (Fig. S7). The results show that the output power of the fibers increases with decreasing temperature to zero and then reaching a constant value (Fig. S7f). Therefore, the spun fiber at zero coagulation bath temperature was used for the subsequent ion transport measurements.

Note S7. Saturation

After the fibers are exposed to the electrolyte solution, fibers are saturated with ions and improve membrane voltage. This saturation can be related to the ion intercalation and pinning via functional groups of negatively and positively charged MXene flakes. To study saturating, we used a concentration gradient of KCl solution on both sides of the fiber. The low concentration side was set at 1 mM, while the concentration of the other side was 1M, and the membrane voltage was recorded in the asymmetric condition of the electrolyte. After about 500 cycles, the voltages of fibers reach a fixed value. Also, we immersed the MXene fibers in KCl solution (0.01 M) for 24 hours and then performed the same test. As shown in Fig. S10, the immersed fiber stabilizes in fewer cycles than the without immersed fiber. Therefore, to ensure saturation of fibers, we soaked the MXene fibers in KCl solution (0.01 M) for 24 hours and then performed ion transport measurements.

Note S8. The surface charge density of nanosheets

The surface charge density σ is obtained by equation S5 [6]:

$$\sigma = \frac{\varepsilon \varepsilon_0 \zeta}{\lambda_d} \tag{S5}$$

where ε_0 and ε are the vacuum permittivity dielectric and the constant of the pure water, ζ is the zeta potential and λ_d is the Debye length in the electrolyte (equation S6):

$$\lambda_d \sim \sqrt{\frac{4\pi\varepsilon_0\varepsilon_r k_B T}{e^2 I}} \tag{S6}$$

where e is the elementary charged, ε_r is the relative dielectric constant, and I is ionic strength [7]. Debye length is 9.62 nm at 1 mM KCl solution.

Note S9. Number of nanochannel inside MXene fiber

A fiber consists of many nanochannels. To obtain this number can be assumed cylindrical fiber with radius (r) as rectangular parallelepiped with the W=$2\pi r$ (width), H=r/2 (height), and L (length) equal to that of the cylinder (Fig. S14) [3]. Therefore, the number of the existing channels estimate by dividing H by the interlayer spacing (h). Our work's average number of nanochannels was ~5.6×10^3 and ~3×10^3 for N-MF and P-MF, respectively.

Note S10. Ion conductivity and ion resistivity

Ion conductivity (κ) and ion resistivity (ρ) for a single nanochannel are calculated as follows:

$$\kappa = \frac{Gl}{wh} \tag{S7}$$

$$\rho = \frac{1}{\kappa} \tag{S8}$$

where G is ionic conductance, h, w, and l are the nanochannel's height, width, and length.

Note S11. Surface charge density and height of nanochannel

The ionic conductance (G) is extracted by equation S9 [8]:

$$G = Ze\left(\mu^+ + \mu^-\right)CN_A\frac{wh}{l} + 2\frac{\sigma w\mu^+}{l} \tag{S9}$$

where Z is cation valence, μ_+ and μ_- are the cation and anion mobility, C is the reservoirs ionic concentration, and N_A is the Avogadro's number. As shown in equation 5, the conductance of nanochannel has two parts of contribution. The first term is the bulk solution conductance, and

the second is the surface charge governed conductance. Due to the Debye length dependence on the ionic concentration, ionic conductivity is close to the bulk value at high concentrations (> 1 mM) of KCl solution. In the bulk conductance regime, the Debay layer's thickness is smaller than the channel's height, and no diffusive layer is overlapping. However, at low concentrations, the ionic conductivity is governed by the surface charges because the dimension of nanochannels is close to Debye length, and consequently, the bulk part of conductance in equation S9 can become negligible, and ion conductance can simplify to:

$$G = 2\frac{\sigma w \mu^+}{l} \tag{S10}$$

and surface charge density of the nanochannel can be obtained by calculating μ^+ and number of channels. Nanochannel height can also be calculated by simplifying equation S7 at low concentrations [9]:

$$k = \frac{2\sigma\mu^+}{h} \tag{S11}$$

Note S12. Redox potential

The measured open-circuit voltage (V_{OC}) contains two parts: the membrane potential (V_m) that is generated by ion selectivity of membrane and redox potential (V_{redox}) that is produced from inequality of chloride concentration at surfaces of electrodes and can obtain by measuring the potential without the MXene membranes (micro size hole (~500μm)) (Fig. S16 and S17) [10]. So, V_m and I_m are calculated by following equations S12 and S13 [11]:

$$V_m = V_{OC} - V_{redox} \tag{S12}$$

$$I_m = \frac{V_m}{V_{OC}} \times I_{SC} \tag{S13}$$

Note S13. Cation transference number

Cation transference numbers vary from unity for an ideal cation-selective membrane to zero for an ideal anion-selective membrane. The cation transference number is calculated according to equation S14 [12]:

$$t_+ = \frac{1}{2}\left(\frac{V_m}{\frac{RT}{ZF}ln\left(\frac{\gamma_H c_H}{\gamma_L c_L}\right)} + 1\right) \tag{S14}$$

where F is Faraday constant, T represents temperature, R is the gas constant, Z denotes charge valent, γ is activity coefficient of ions, and c_H and c_L signify high and low ion concentrations, respectively.

Note S14. Mobility

The mobility ratio could be calculated as [13]:

$$\frac{\mu^+}{\mu^-} = -\left(\frac{Z_+}{Z_-}\right)\frac{\left(\ln(\Delta) - Z_-\frac{FV_m}{RT}\right)}{\left(\ln(\Delta) - Z_+\frac{FV_m}{RT}\right)} \tag{S15}$$

where Z_+, Z_- are the valences of cations and anions, respectively, F is the Faraday constant, R is the universal gas constant, T=295K, Δ is the concentration gradient on both sides of the membrane. Assuming the effect of surface charge density at high concentrations is negligible, the ionic conductivity can be described as:

$$\kappa \approx F\left(C_+\mu^+ + C_-\mu^-\right) \tag{S16}$$

where C_+, and C_- are the concentrations of cations and anions, respectively. Using both (S15) and (S16) equations, μ^+ and μ^- can be calculated.

Note S15. Energy barriers

The overall energy barrier for ion transport through subnanometer channels is involved partitioning energy (ion dehydration) and interachannel diffusion (ion reactions with the channel wall). As the ion dehydration increases, the probability of ions entering the channel decreases. Furthermore, during interachannel diffusion of ions, counter-ions (the opposite charge as the channel) hop between surface charge positions, and co-ions (same charge of the channel) bypass the functional groups. Therefore, changing the channel's height and surface charge density will affect partitioning energy and interachannel diffusion, respectively [14].

Note S16. pH

Pure Ti_3C_2 blocks are positively charged and neutralized by terminations. In an aqueous solution, deprotonation of hydroxyl groups leads to negative charge on MXene surface, following a chemical equilibrium [15]:

$$(Ti_3C_2)_n\,(OH)_x\,(O^-)_y\,F_z + aH_2O \leftrightarrow (Ti_3C_2)_n\,(OH)_{x-a}\,(O^-)_{y+a}\,F_z + aH_3O^+ \quad \text{(S17)}$$

H^+ ions protonate the functional groups at low pH, and the resulting reaction shifts towards the left. But at high pH, the presence of OH^- ions develops deprotonation and negative surface charge on MXene flakes.

PDDA, a long-chain cationic surfactant, is neutralized by bonding nitrogen and chlorine. When positively MXene flakes are placed in neutral water, ionization of PDDA results in positive charges on MXene sheets, resulting in the following equilibrium:

$$(C_8H_{16})_n\,(NCl)_x\,(N^+)_y + aH_2O \leftrightarrow (C_8H_{16})_n\,(NCl)_{x-a}\,(N^+)_{y+a} + aHCl + aOH^- \quad \text{(S18)}$$

At high concentrations of H^+ (low pH), the amount of chlorine loss increases, leading to a rise in the number of N^+. But at high pH, the bonding between OH^- ions and N^+ ions reduce the surface charge of positively MXene.

Note S17. Electrochemical parameters

The permselectivity (α) of membrane could be acquired by equation S19 [16]:

$$\alpha = \frac{V_{Exp}}{V_{theory}} \times 100\% \quad \text{(S19)}$$

where V_{Exp} is the measured membrane potential, and V_{theory} is the membrane's theoretical potential, which could be obtained from the Nernst equation assuming complete membrane permselectivity. The electrochemical energy conversion efficiency (η), defined as ratio of the output energy (electrical energy of the cell) to the input energy (Gibbs free energy), can be calculated as follows:

$$\eta_{maxw} = \frac{1}{2}\left(\frac{V_{Exp}}{V_{theory}}\right)^2 \times 100\% \quad \text{(S20)}$$

Note S18. Numerical simulation

The numerical simulation of ion transport behavior in MXene fiber channels under two configurations was calculated by COMSOL Multiphysics (a commercial finite-element software package). This simulation was carried out using a two-dimensional Poisson-Nernst-Planck (PNP) model and considering appropriate boundary conditions. The Nernst-Planck equation is the flux equation for each ion species that physically describes a charged nanochannel's transport properties. Nernst-Planck equation is shown below:

$$j_i = -D_i \nabla C_i - \frac{z_i F}{RT} D_i c_i \nabla \varphi \quad \text{(S21)}$$

Where j_i is the ionic flux, c_i is the ion concentration, D_i is the diffusion coefficient, z_i is the valence number for each species, R is the universal constant, F is Faraday constant, T is the absolute temperature, and φ is the electrical potential.

The relationship between the ion concentrations and electric potential describe by the Poisson equation:

$$\nabla^2 \varphi = -\frac{F}{\varepsilon} \sum z_i c_i \quad \text{(S22)}$$

Where ε is the permittivity of the electrolyte.

Generally, the system can simplify by assuming steady-state conditions, so the flux should be time-independent with the below equation when the system reaches a stationary regime:

$$\nabla \cdot j_i = 0 \tag{S23}$$

Fig. S26 and S27 show the numerical simulation model. It contains nanochannel with the length of 50 nm and the width obtained from the experiment, 4.7Å for negative MXene channel and 9.2 Å for positive MXene channel. Reservoir (40nm × 20nm) was added to minimize the effect of mass transfer resistance at the entrance and exit on the overall ionic transport.

We did not apply any voltage difference at the reservoirs to obtain the osmotic short-circuit current, and the ionic current, I, across the reservoirs and nanochannel was calculated by:

$$I = \int_s F\left(z_p J_{p+} z_n J_n\right) \cdot n\mathrm{d}S \tag{S24}$$

At boundaries, the ion flux has zero normal components:

$$n \cdot j_i = 0 \tag{S25}$$

The electrostatic boundary condition for the potential φ is given by:

$$n \cdot \nabla\varphi = -\frac{\sigma}{\varepsilon} \tag{S26}$$

where σ and n represent the surface charge density of the walls and the unit normal vector to the wall surface. The surface charge density on the walls of the reservoirs was zero, and according to the experimental results, surface charge density was -1.68 mC m^{-2}, and 3.52 mC m^{-2} for the negative and positive channels, respectively.

The simulation was performed with two configurations. Variable surface charge design: two reservoirs under 1000 folds (1M/1mM) of KCl concentration gradient and NP-MF cell design: three reservoirs 50 folds (0.5M/0.01M) of NaCl.

Supplementary Figures

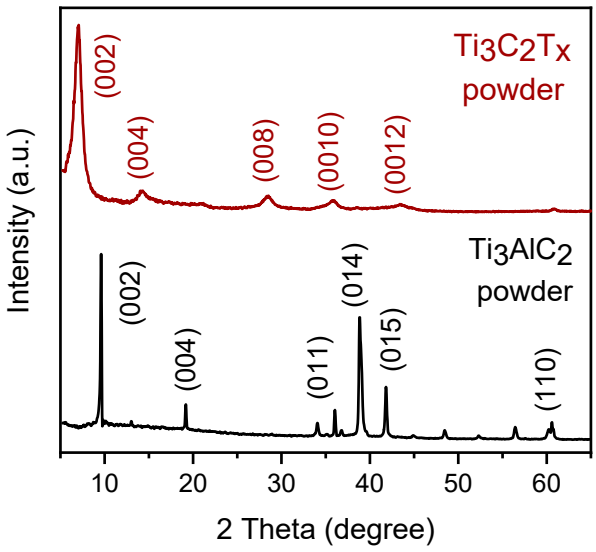

Fig. S1. X-ray diffraction (XRD) patterns of Ti_3AlC_2 MAX powder and $Ti_3C_2T_x$ MXene powder.

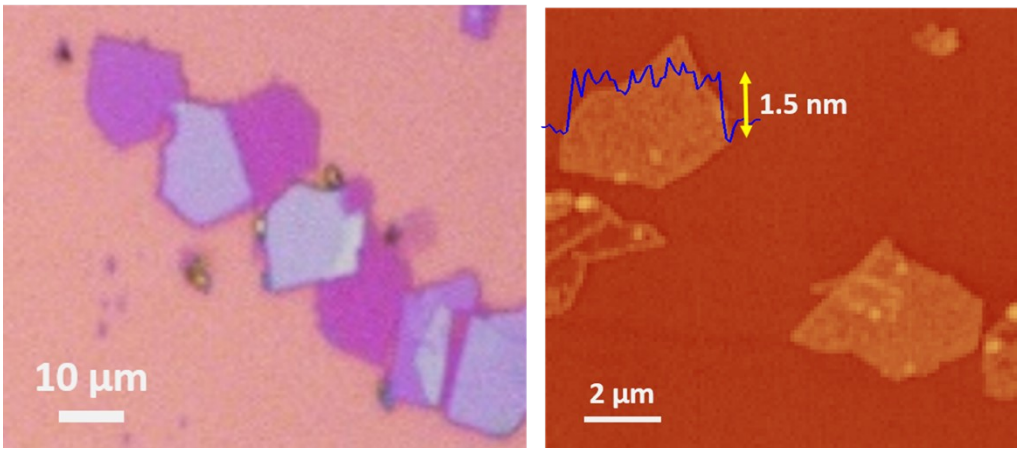

Fig. S2. Atomic Force Microscopy (AFM) image and height profile of $Ti_3C_2T_x$ flakes.

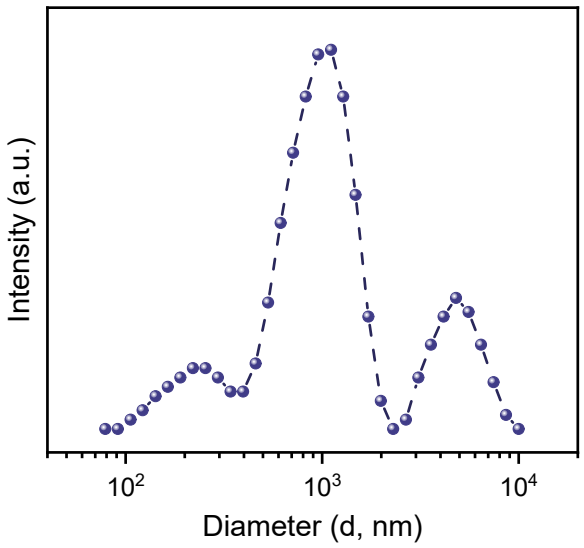

Fig. S3. Size distribution of $Ti_3C_2T_x$ flakes in aqueous dispersions was obtained using the dynamic light scattering (DLS) technique.

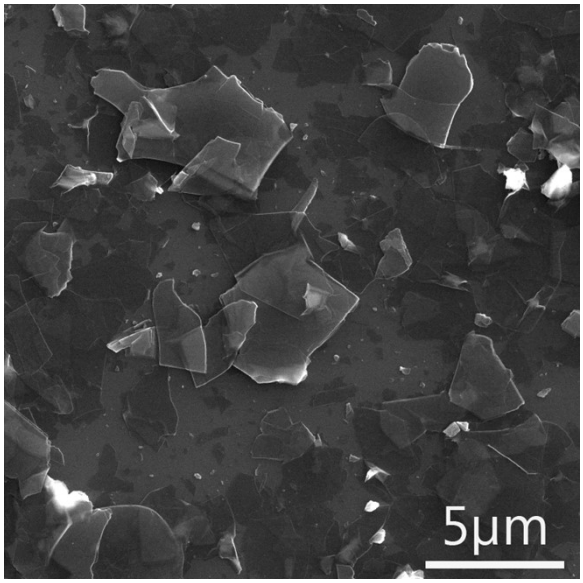

Fig. S4. Scanning electron microscopy (SEM) image of $Ti_3C_2T_x$ flakes on a silicon wafer.

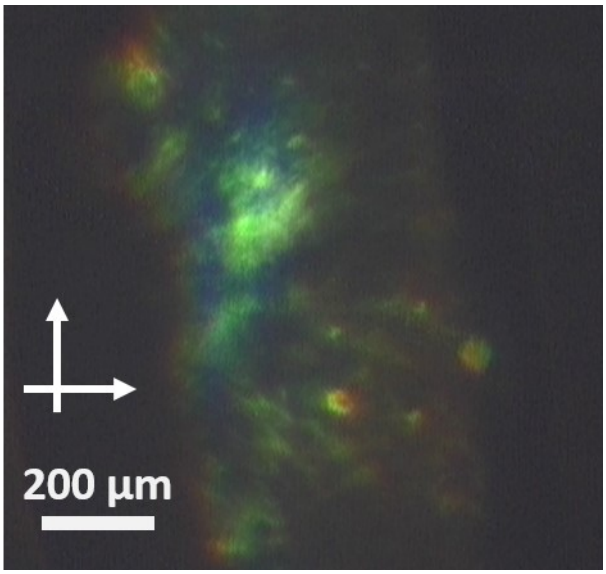

Fig. S5. Polarized optical microscopy (POM) images of $Ti_3C_2T_x$ flakes dispersions illustrate its liquid-crystalline phase.

Fig. S6. Optical images for N-MX flakes in IPA and water.

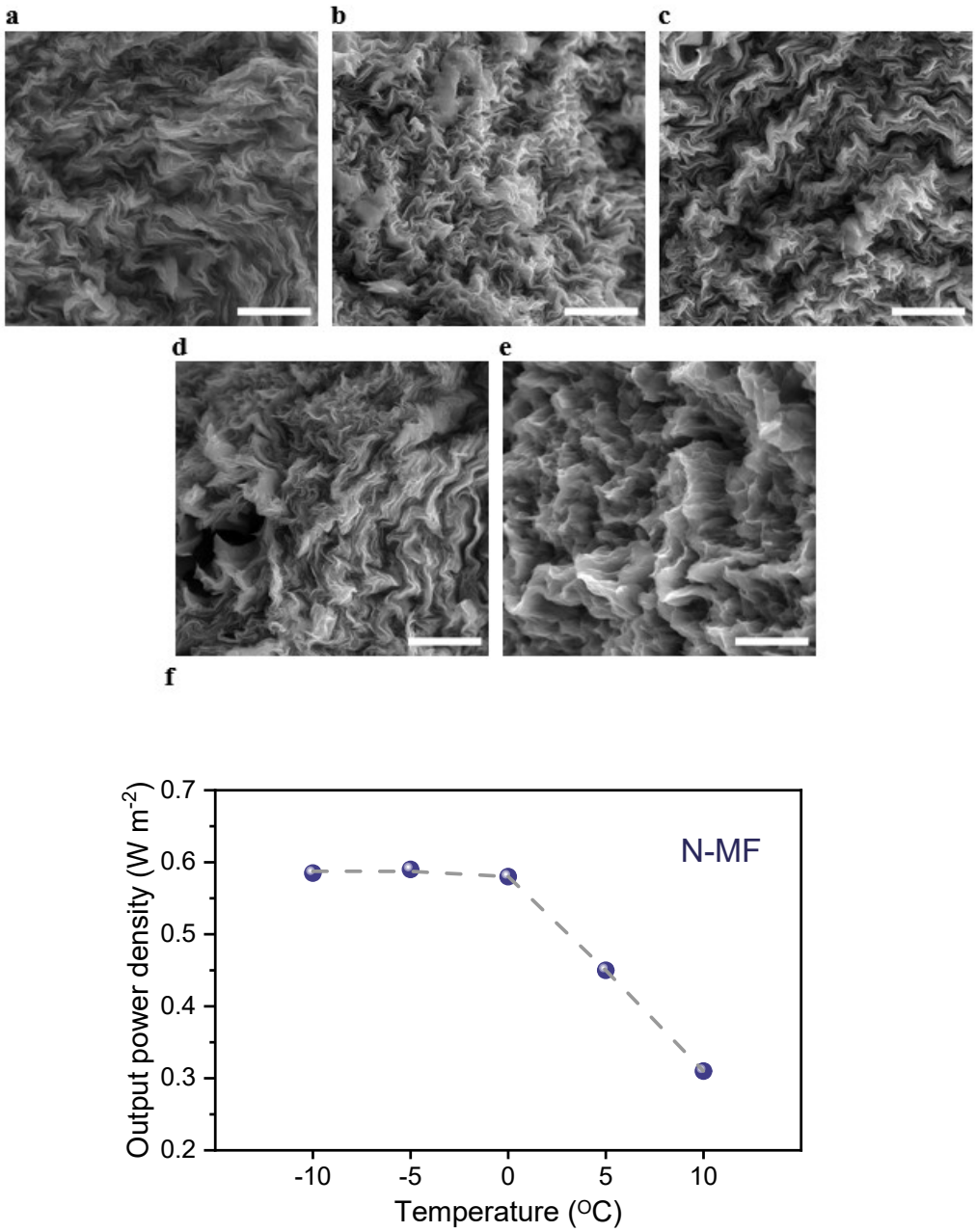

Fig. S7. SEM images and output power density of N-MF at several temperatures. Cross-section SEM images for N-MF at (a) -10℃, (b) -5℃, (c) 0℃, (d) 5℃ and (e) 10℃ coagulation bath (scale bar, 5 μm). (f) The output power density of N-MF for various temperatures under concentration gradient 10 folds of KCl.

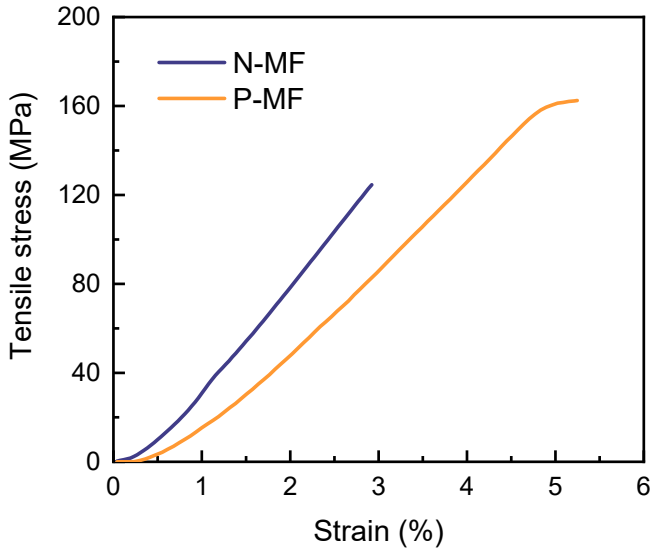

Fig. S8. Tensile stress-strain curves of N-MF and P-MF. The cross-sectional area of all fibers was calculated from the SEM images.

a)

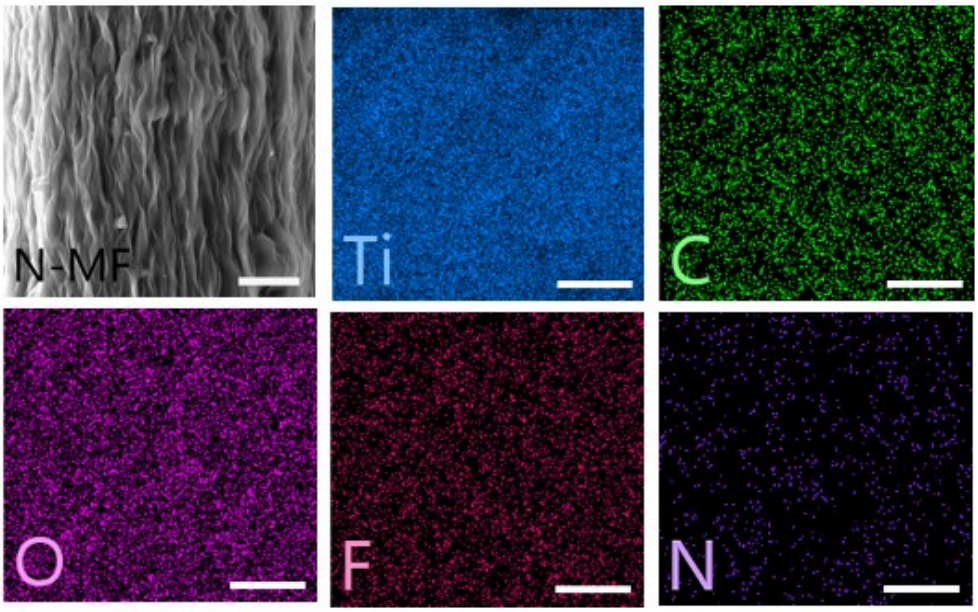

b)

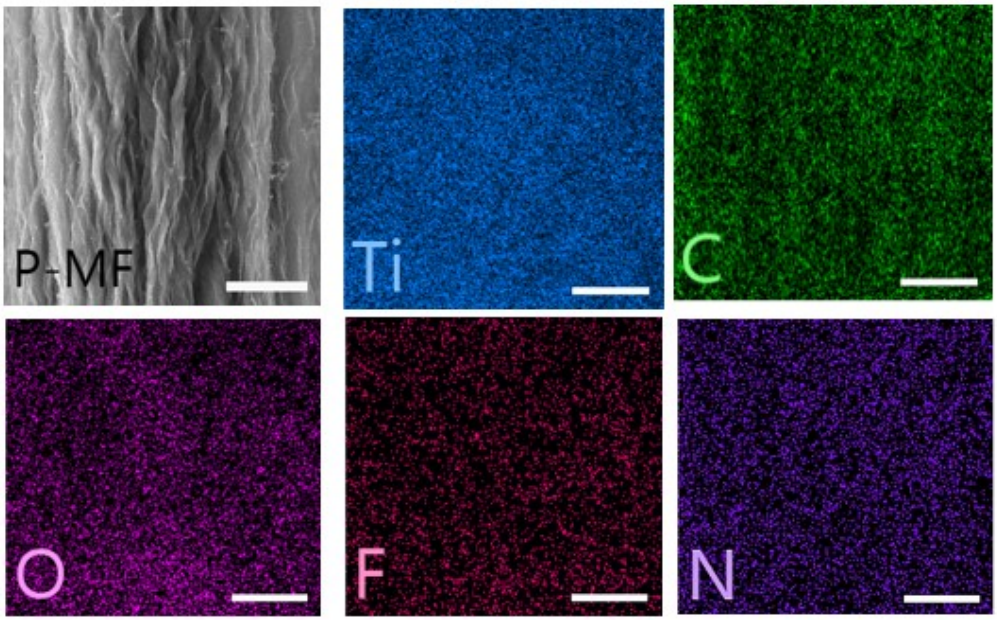

Fig. S9. SEM images and corresponding EDX mapping of the element distribution. (a) N-MF and (b) P-MF (scale bar, 5 μm).

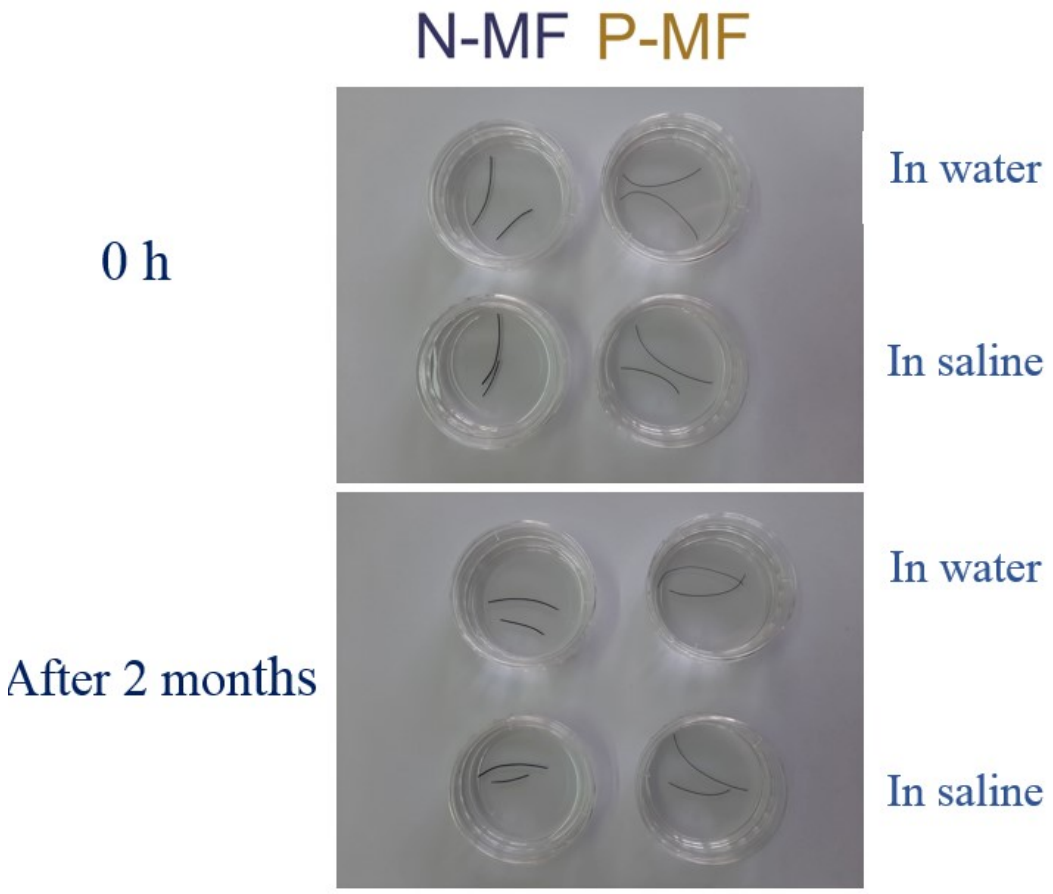

Fig. S10. The stability of the N-MF and P-MF in water and in saline for two months.

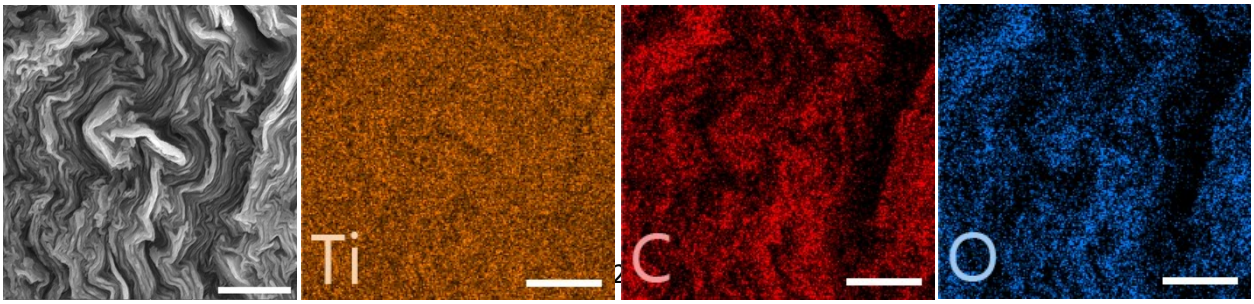

a

b

c

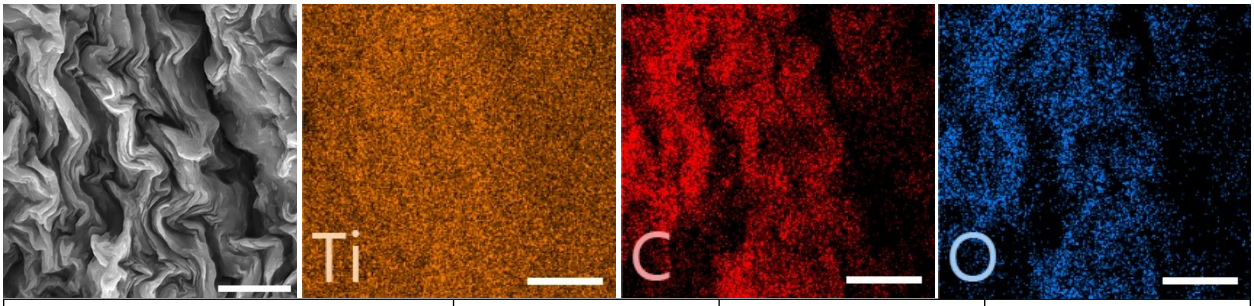

Sample	Ti (Wt%)	C (Wt%)	O (Wt%)
Fresh N-MF	58.6	25.5	15.9
N-MF after immersed in saline (for two months)	57.5	26.3	16.2

Fig. S11. SEM images and corresponding EDX mapping of the element distribution N-MF for (a) fresh and (b) after immersed in saline for two months (scale bar, 2 μm). (c) Atomic concentration of elements on the cross-section of fresh N-MF and salt solution-immersed N-MF.

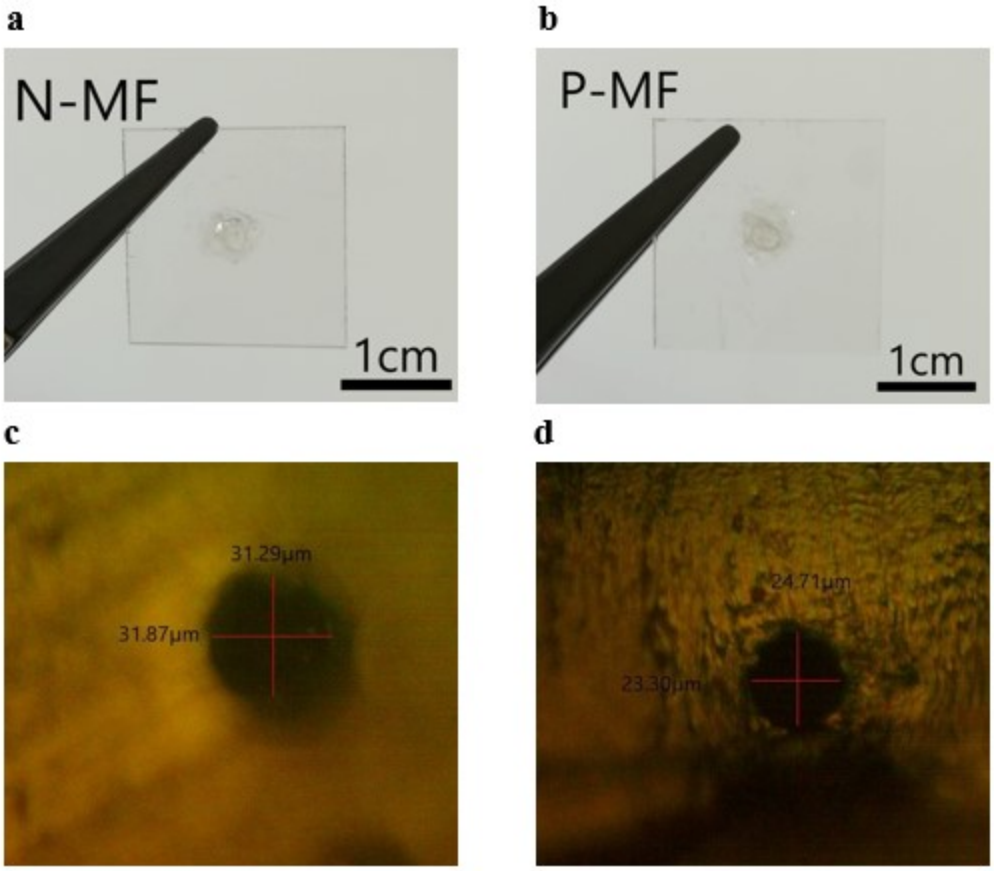

Fig. S12. Optical images of fibers. Photographs of the N-MF (a, c) and P-MF (b, d) fiber membranes embedded into a circle slot within a plastic plate with a thickness of 1mm using epoxy. (scale bar, 20 μm)

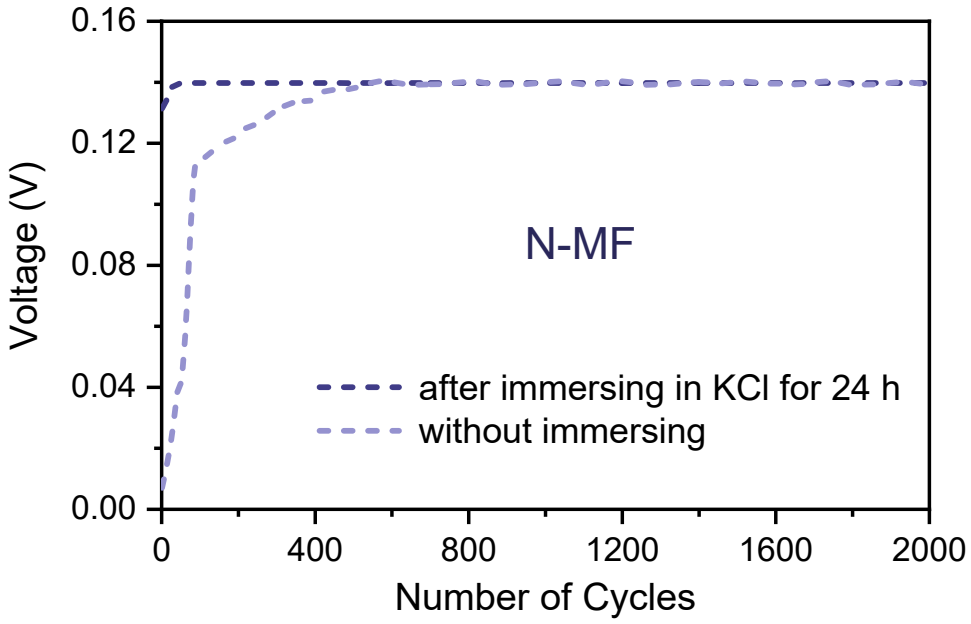

a

b

Fig. S13. Effect of saturation on voltage. Membrane voltage (a) N-MF and (b) P-MF with respect to time under a concentration gradient of 10^3 with and without immersing in KCl.

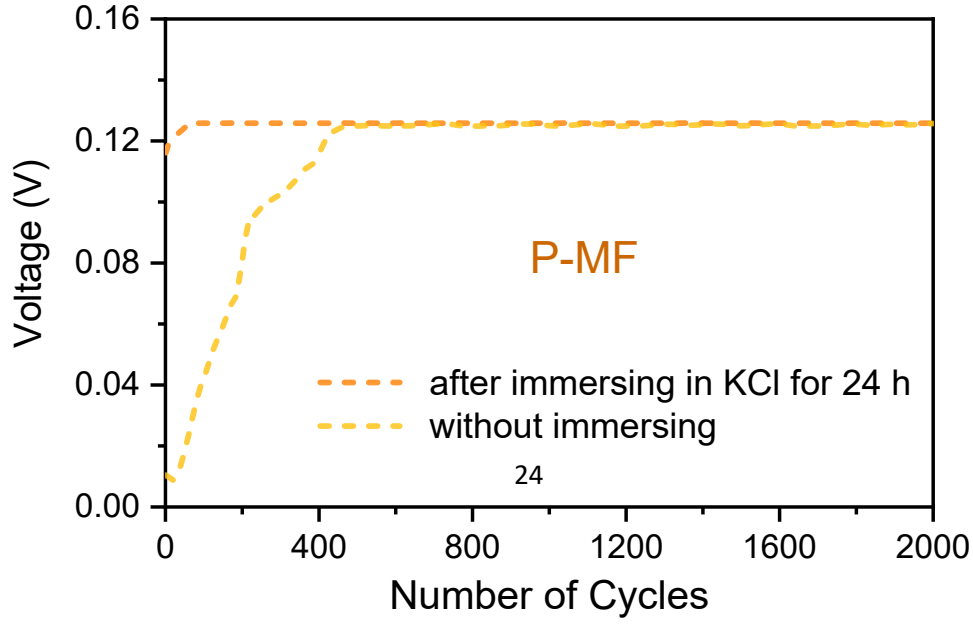

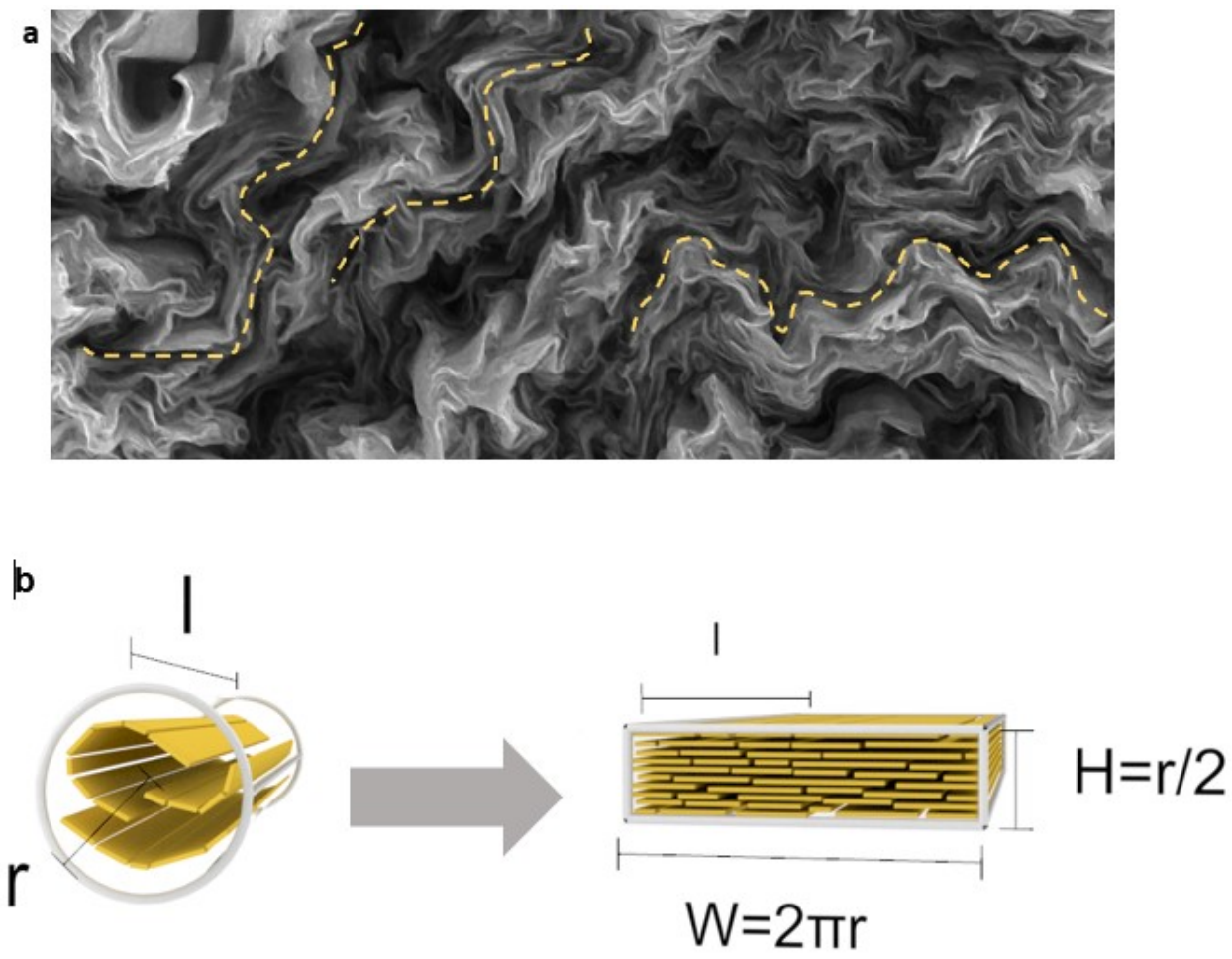

Fig. S14. Modeling of MXene fiber nanochannels to MXene film. (a) Cross-section SEM image of N-MF. Some curved 2D nanochannels in the MXene fiber are marked with dotted lines. (b) Schematic illustration showing the re-assembly of nanochannels confined in a cylindrical fiber with radius (r) into a rectangular parallelepiped as is performed for MXene films.

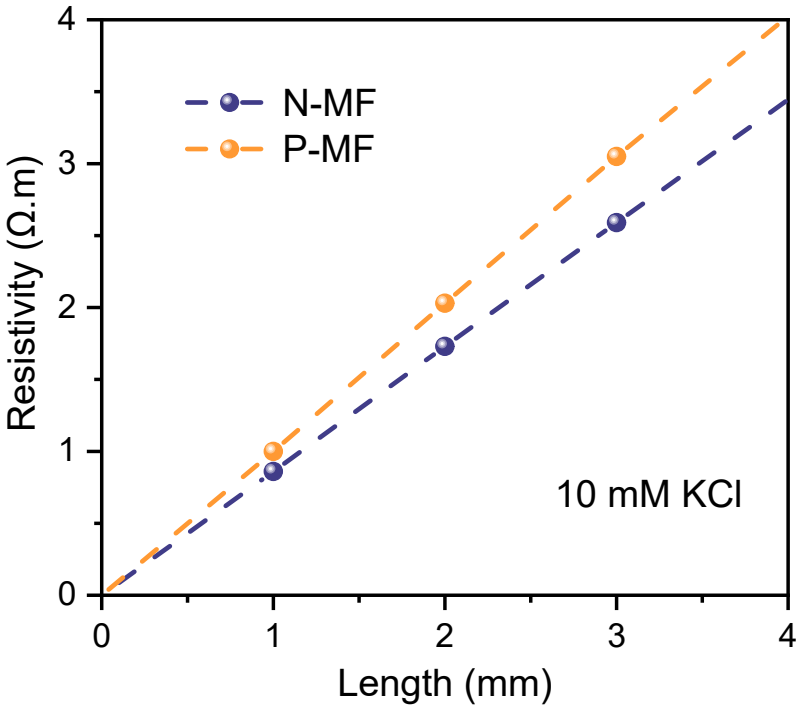

Fig. S15. Resistivity for various lengths of MXene fibers in 10 mM KCl solution.

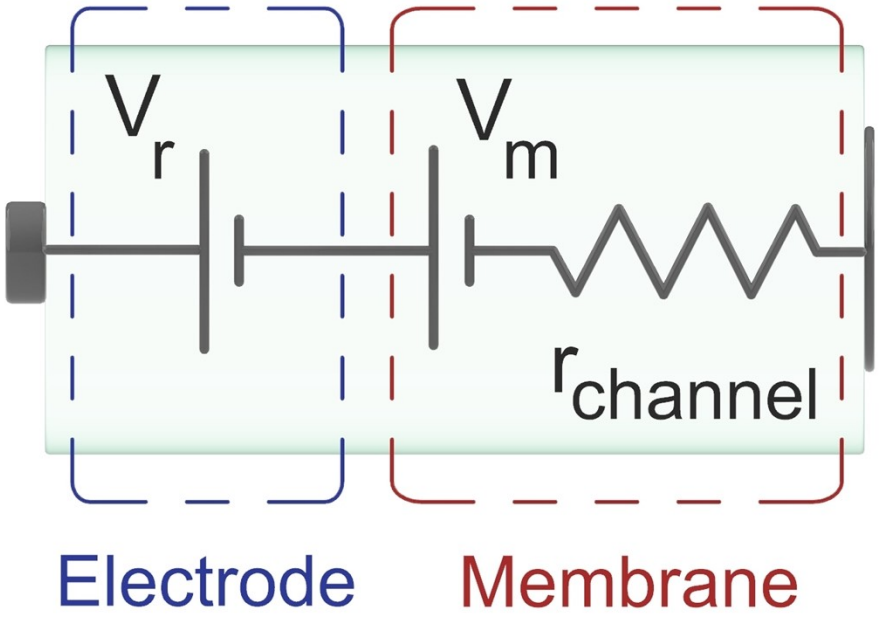

Fig. S16. Schematic of an equivalent circuit for power generation. The measured potential (V_{OC}) is composed of membrane potential (V_m) and redox potential (V_{redox}).

a

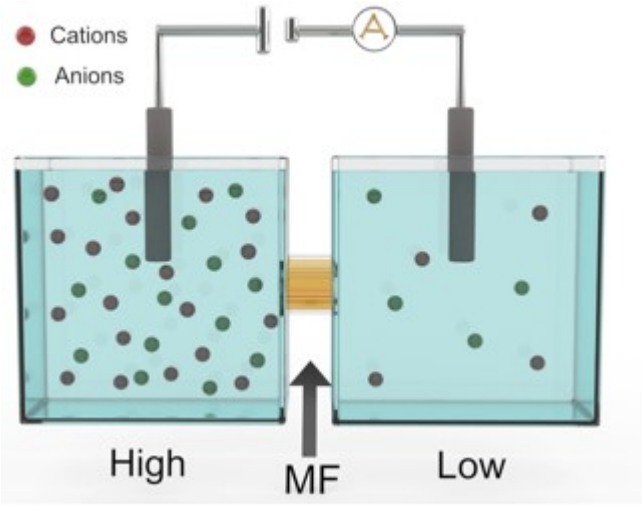

b

Concentration gradient	1mM/10mM	1mM/50mM	1mM/0.1M	1mM/0.5M	1mM/1M
V_{redox} (mV)	46.7	73.8	103.1	127.2	148.7

Fig. S17. Experimental setup for measuring redox potential and the corresponding measured data. **(**a) Schematic of the experimental setup for measuring redox potential of electrodes. (b) Measured data of redox potential under various concentration gradients.

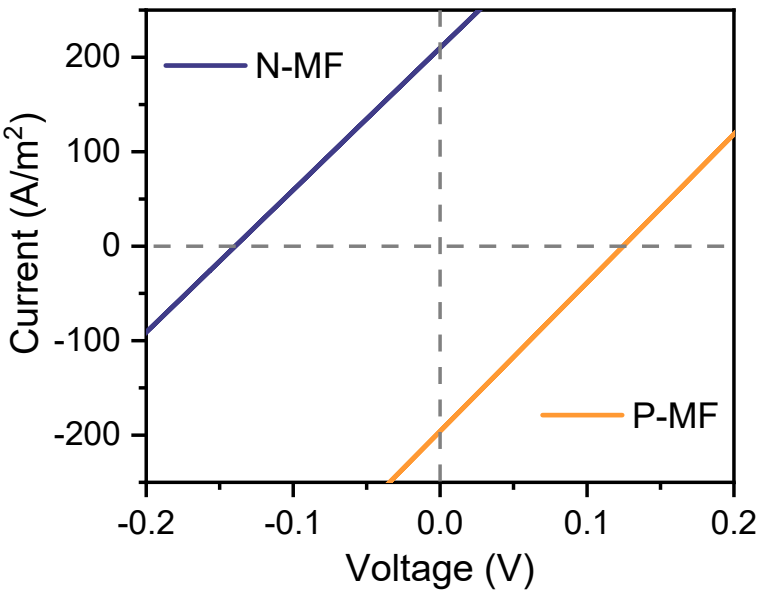

Fig. S18. Opposite polarity V_{OC} and I_{SC} of the positively and negatively MXene fibers under the salinity concentration gradient of 1000 folds (1M/10^{-3}M).

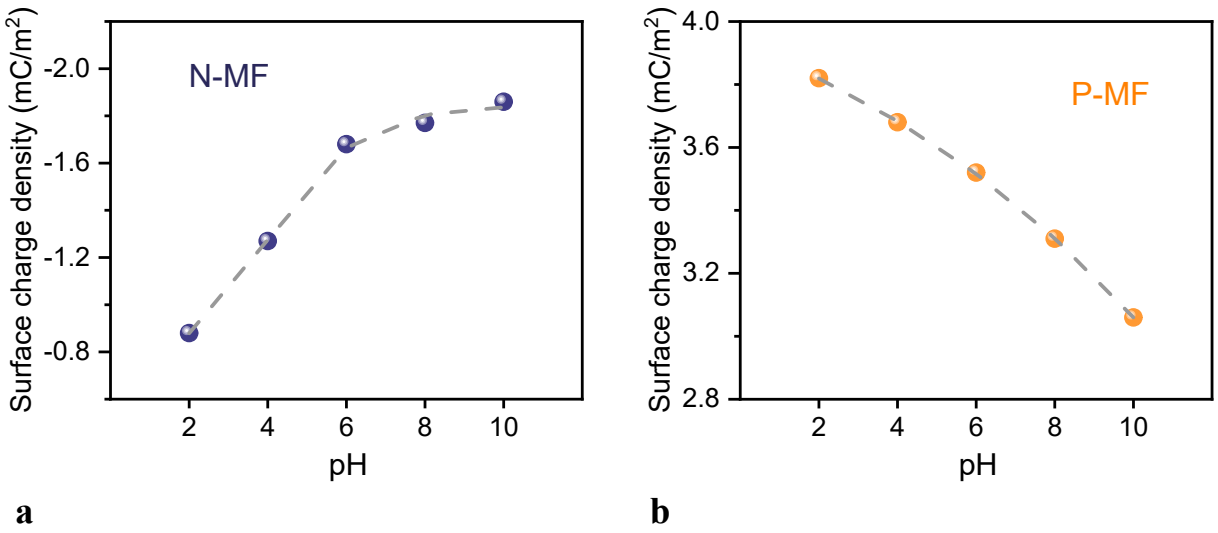

Fig. S19. Nanochannel surface charge density of (a) N-MF and (b) P-MF as a function of pH.

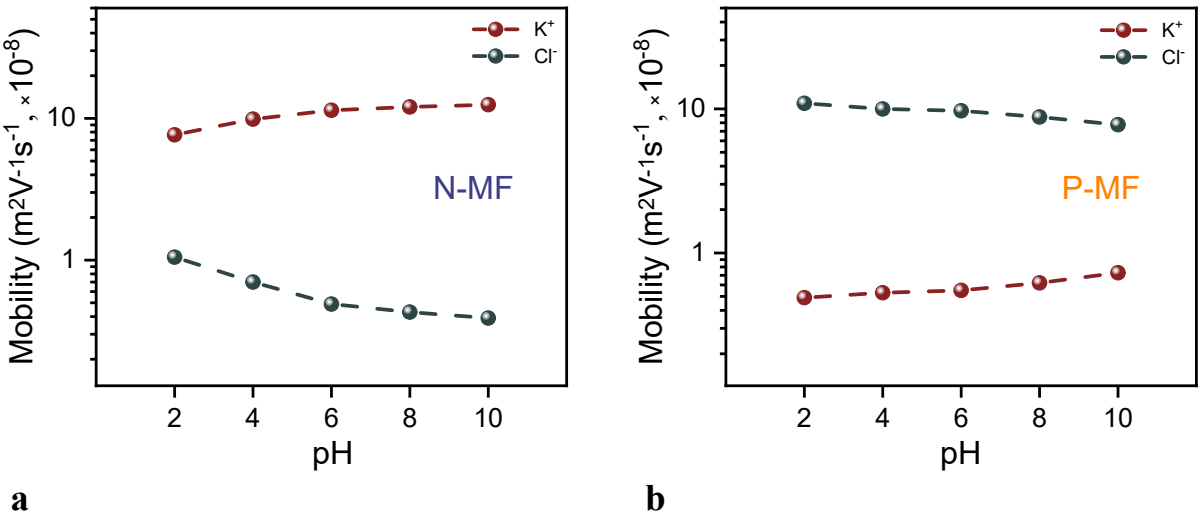

Fig. S20. Ion mobility of K^+ and Cl^- for (a) N-MF and (b) P-MF as a function of pH.

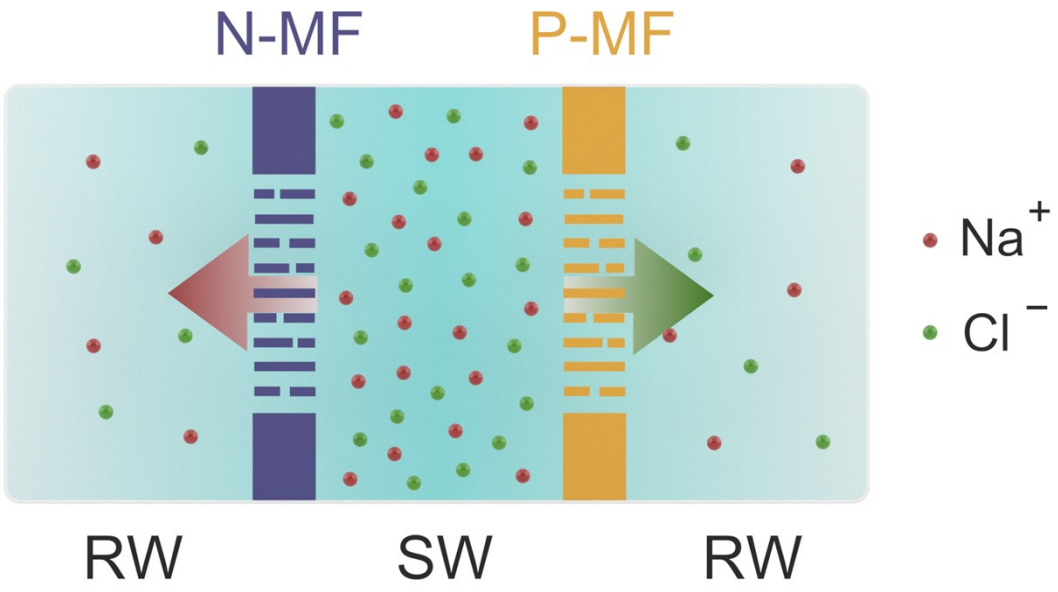

a

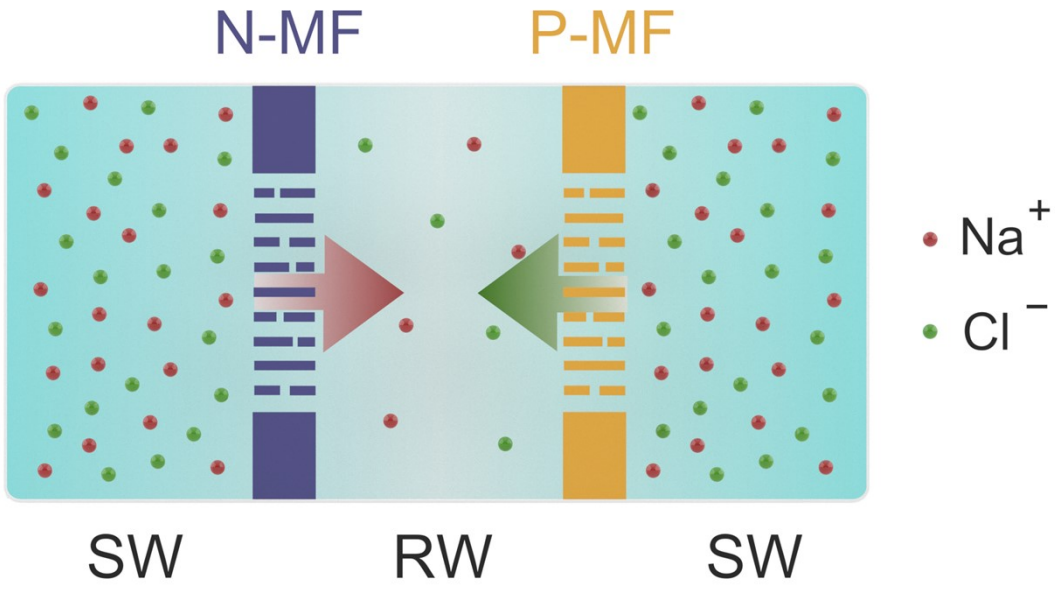

b

Fig. S21. Schematic of two configurations for injecting the electrolyte solutions. **(**a) RW|N-MF|SW|P-MF|RW, (b) SW|N-MF|RW|P-MF|SW.

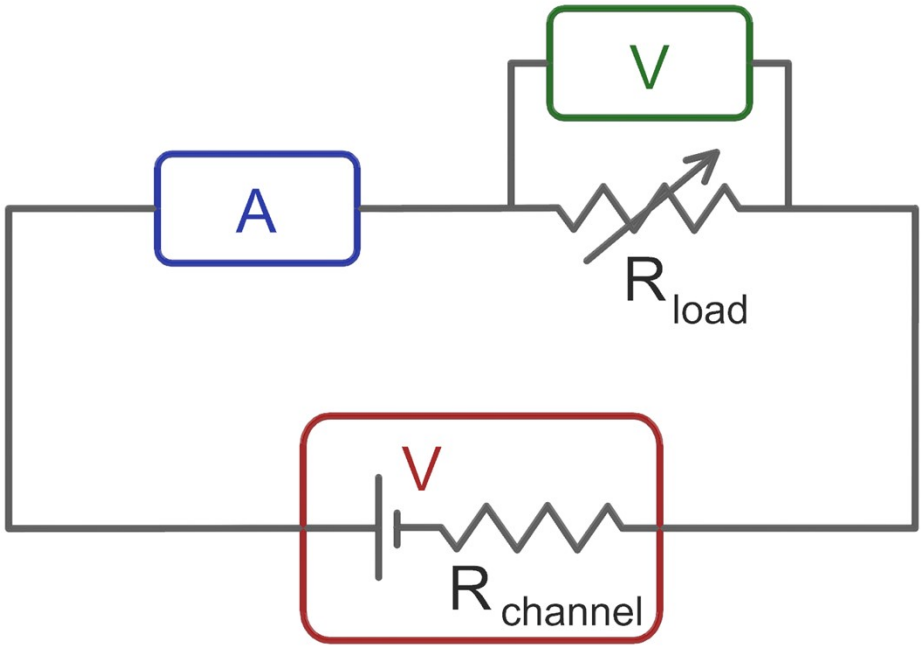

Fig. S22. Diagram of an external circuit to supply an electronic load resistance for measuring harvested osmotic power.

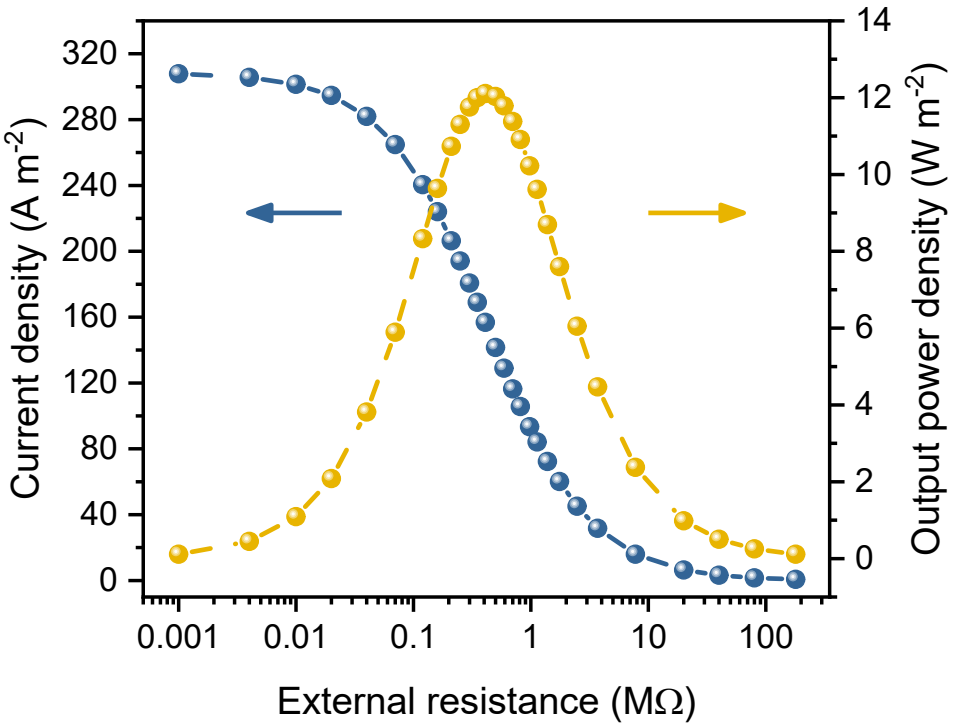

Fig. S23. The current density and output power density of the NP-MF cell as a function of the load resistance under configuration I and using natural seawater and river water. The current density decreases by increasing of ionic resistance, while the power density reaches to maximum value of ~12.1 W m^{-2}.

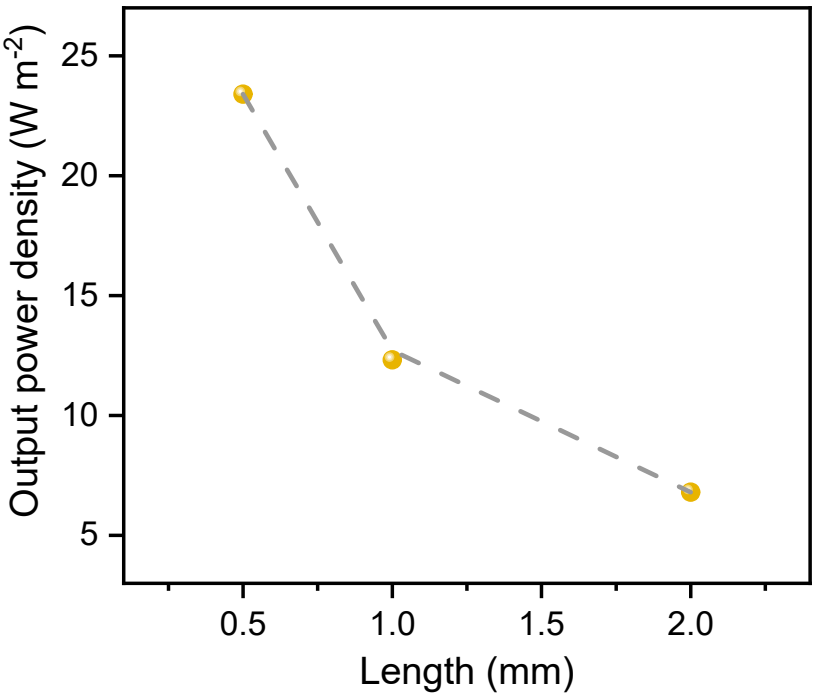

Fig. S24. Output power density for various lengths of NP-MF cell between artificial river water (0.01 M NaCl) and seawater (0.5 M NaCl).

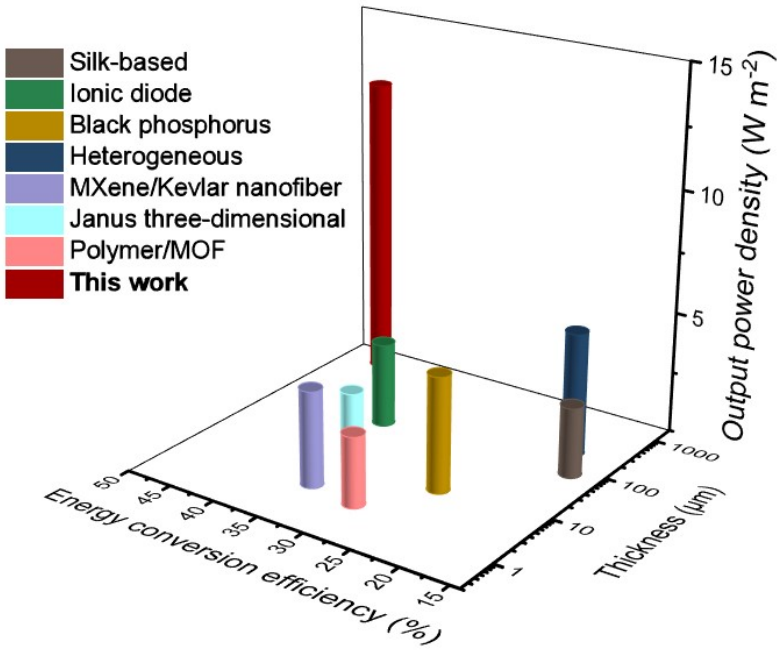

Fig. S25. Comparison of power generation performance of the NP-MF cell with the state-of-art membrane-based osmotic power harvesters as a function of thickness (0.5 M/0.01 M NaCl).

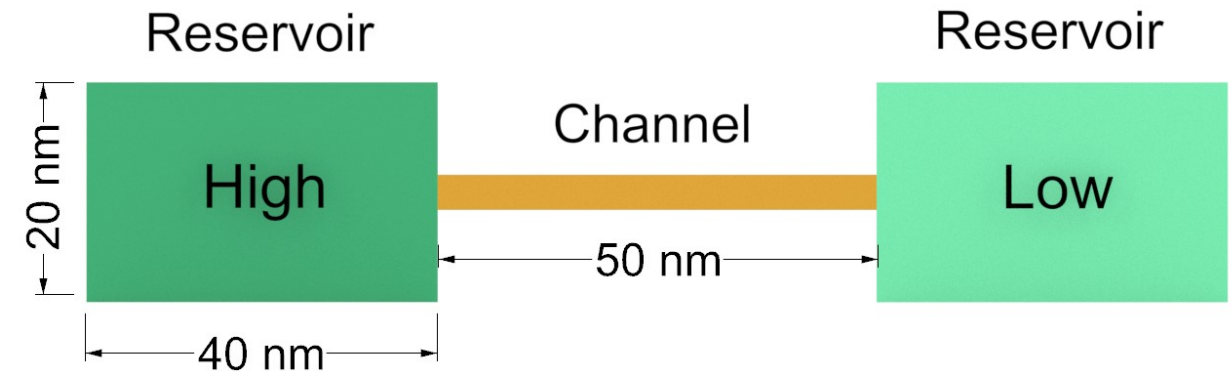

a

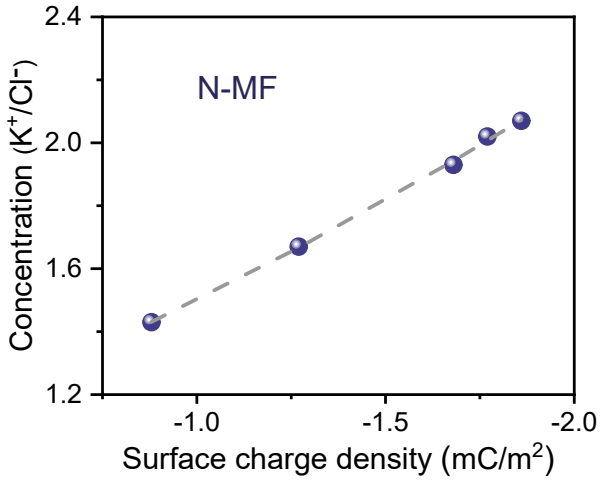

b

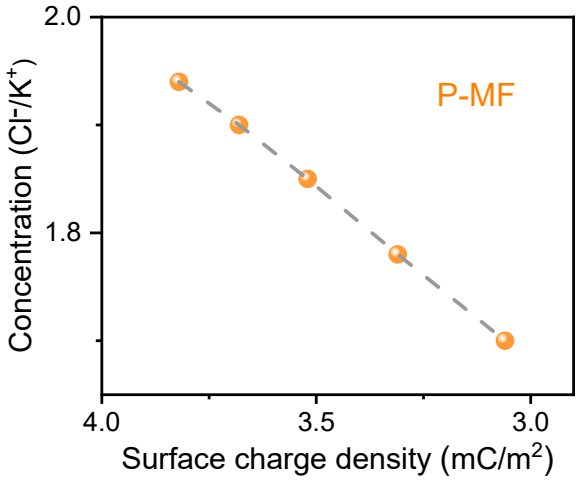

c

Fig. S26. Model and results of variable surface charge simulation. (a) The design of numerical simulation with two reservoirs. The surface charge density and channel height used in the simulation were obtained from the experimental section. The scale has not been considered in the drawing. Result simulation of (b) concentration (K^+/Cl^-) and c) concentration (Cl^-/K^+) in a negative and positive nanochannel, respectively, as a function of surface charge density. Nanochannel surface charge density was variable based on pH.

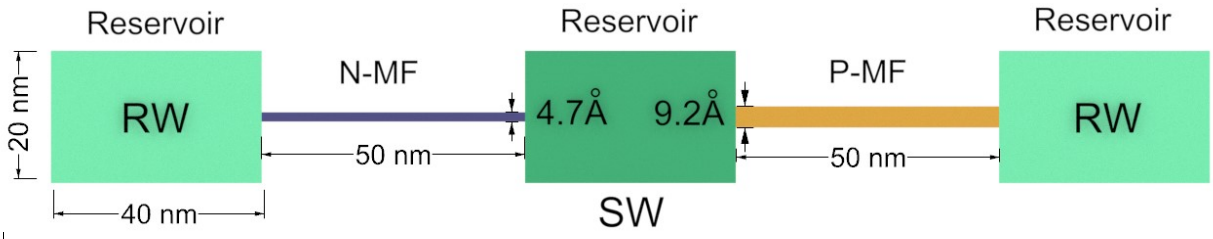
Reservoir
Reservoir
Reservoir
RW
N-MF
4.7Å
9.2Å
P-MF
RW
20 nm
50 nm
50 nm
40 nm
SW

a

b

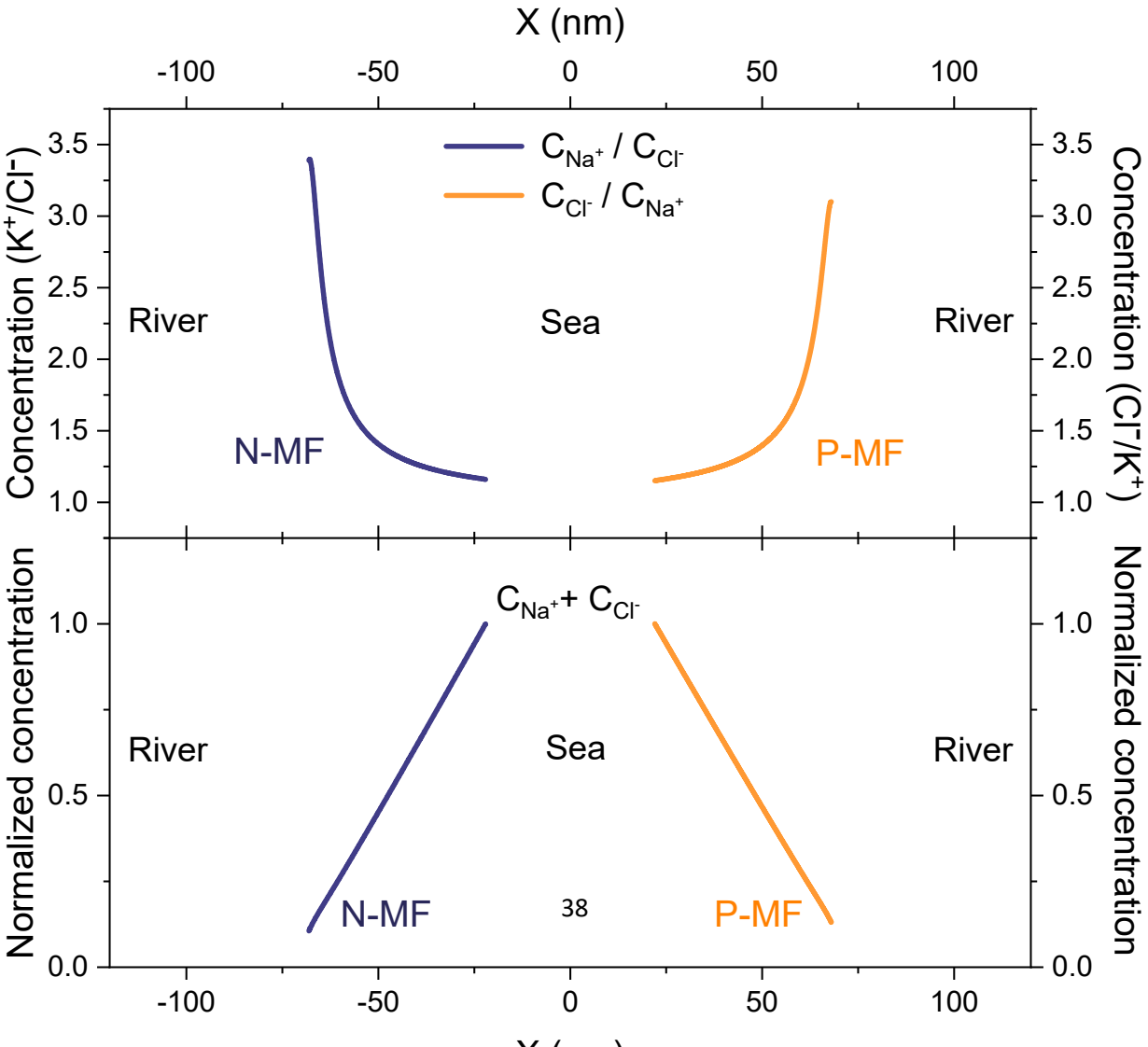
X (nm)
-100
-50
0
50
100
Concentration (K+/Cl-)
Concentration (Cl-/K+)
3.5
3.0
2.5
2.0
1.5
1.0
CNa+ / CCl-
CCl- / CNa+
River
Sea
River
N-MF
P-MF
Normalized concentration
1.0
0.5
0.0
CNa+ + CCl-
River
Sea
River
N-MF
P-MF
38

Fig. S27. Model and results of NP-MF cell simulation. (a) The design of numerical simulation with three reservoirs. The surface charge density and channel height used in the simulation were obtained from the experimental section. The scale has not been considered in the drawing. (b) Result simulation of concentration (K^+/Cl^-), concentration (Cl^-/K^+), and normalized concentration along the negative and positive nanochannel length.

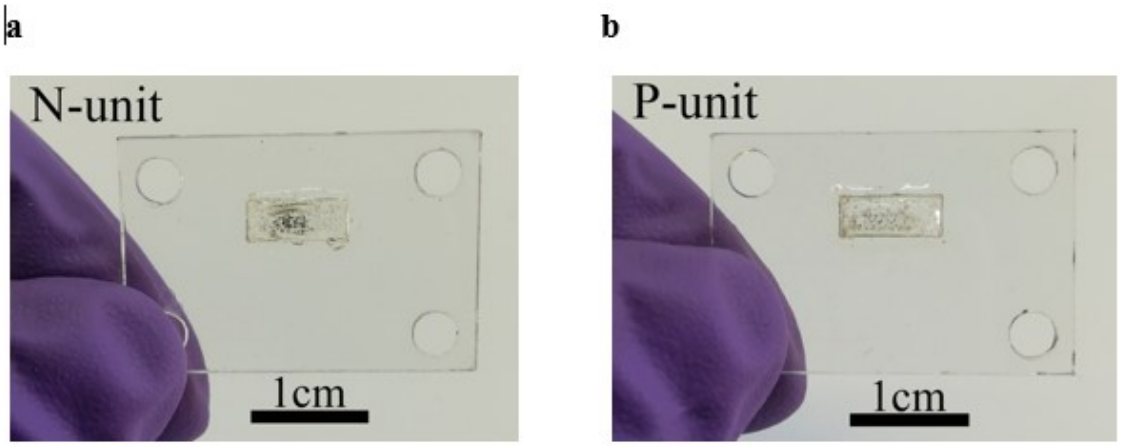

Fig. S28. Optical image of a unit of fiber. Photographs from the collection of 50 (a) N-MF and (b) P-MF fibers embedded into a rectangular slot within a plastic plate using epoxy for making NP-unit cell.

Supplementary Tables

Table S1. Hydration enthalpy, ionic and hydrated radii of ion species

Ions	Ionic radius (nm)	Hydrated radius (nm)	Enthalpy of hydration (kJ mol^{-1})
K^+	0.149	0.331	−338.9
Na^+	0.117	0.358	−422.6
Ca^{2+}	0.100	0.412	−1615.0
Fe^{3+}	0.069	0.457	−4418.3
Cl^-	0.164	0.332	−351.5

Table S2. Comparison of the performance of the oppositely charged MXene fiber membranes with state-of-the-art membranes.

Membrane types	Salinity gradient	Thickness	Efficiency (%)	P_{max} (W/m^2)	Ref.
Oppositely Charged MXene fibers	0.5 M/0.01 M NaCl	1 mm	**45.7**	**12.3**	This work
Silk-based hybrid membranes	0.5 M/0.01 M NaCl	80 μm	17.2	2.86	[10]
Oppositely charged $Ti_3C_2T_x$ MXene membranes	0.5 M/0.01 M NaCl	-	44.3	4.6	[16]
MXene/Kevlar nanofiber composite	0.5 M/0.01 M NaCl	2 μm	35	3.92	[17]
Graphene oxide membrane	0.5 M/0.01 M NaCl	10 μm	36.6	0.77	[12]
Janus three-dimensional (3D) porous membrane	0.5 M/0.01 M NaCl	11 μm	35.7	2. 66	[18]
Polymer/MOF	0.5 M/0.01 M NaCl	1.6 μm	29.7	2.87	[19]
Ionic diode membrane	0.5 M/0.01 M NaCl	64 μm	37.3	3.46	[20]
Heterogeneous membrane by three-dimensional hydrogel	0.5 M/0.01 M NaCl	210 μm	19.2	5.06	[21]
Aligned Bacterial Cellulose Biofilm	0.5 M/0.01 M NaCl	0.09 mm	36.4	0.23	[22]
Black phosphorus (BP)	0.5 M/0.01 M NaCl	8 μm	25.2	4.7	[23]
Bacterial cellulose biofilms	0.5 M/0.01 M NaCl	-	35.9	2.25	[24]
Biomimetic Nacre-Like Silk-Crosslinked	0.5 M/0.01 M NaCl	-	27.2	5.07	[25]

References

1 A. Kumar, C. Goyal, S. Gautam, S. Ibraheem, T. A. Nguyen and G. Yasin, in *Nanomaterials for Electrocatalysis*, Elsevier, 2022, pp. 23–46.

2 Z. Ling, C. E. Ren, M.-Q. Zhao, J. Yang, J. M. Giammarco, J. Qiu, M. W. Barsoum and Y. Gogotsi, *Proc. Natl. Acad. Sci.*, 2014, **111**, 16676–16681.

3 H. Park, K. H. Lee, Y. B. Kim, S. B. Ambade, S. H. Noh, W. Eom, J. Y. Hwang, W. J. Lee, J. Huang and T. H. Han, *Sci. Adv.*, 2018, **4**, eaau2104.

4 C. Hu, J. Li, D. Liu, R. Song, J. Gu, N. Prempeh and H. Li, *J. Appl. Polym. Sci.*, 2017, **134**, 45463.

5 H. Zhang, X. Lu, Z. Liu, Z. Ma, S. Wu, Z. Li, X. Kong, J. Liu and C. Wu, *J. Memb. Sci.*, 2018, **550**, 9–17.

6 J. Schaep and C. Vandecasteele, *J. Memb. Sci.*, 2001, **188**, 129–136.

7 J. P. Thiruraman, P. Masih Das and M. Drndić, *ACS Nano*, 2020, **14**, 3736–3746.

8 K. Raidongia and J. Huang, *J. Am. Chem. Soc.*, 2012, **134**, 16528–16531.

9 T. Li, S. X. Li, W. Kong, C. Chen, E. Hitz, C. Jia, J. Dai, X. Zhang, R. Briber, Z. Siwy, M. Reed and L. Hu, *Sci. Adv.*, 2019, **5**, eaau4238.

10 W. Xin, Z. Zhang, X. Huang, Y. Hu, T. Zhou, C. Zhu, X. Y. Kong, L. Jiang and L. Wen, *Nat. Commun.*, 2019, **10**, 3876.

11 J. Feng, M. Graf, K. Liu, D. Ovchinnikov, D. Dumcenco, M. Heiranian, V. Nandigana, N. R. Aluru, A. Kis and A. Radenovic, *Nature*, 2016, **536**, 197–200.

12 J. Ji, Q. Kang, Y. Zhou, Y. Feng, X. Chen, J. Yuan, W. Guo, Y. Wei and L. Jiang, *Adv. Funct. Mater.*, 2017, **27**, 1603623.

13 H. Ghanbari and A. Esfandiar, *Carbon N. Y.*, 2020, **165**, 267–274.

14 X. Zhou, Z. Wang, R. Epsztein, C. Zhan, W. Li, J. D. Fortner, T. A. Pham, J.-H. Kim and M. Elimelech, *Sci. Adv.*, , DOI:10.1126/sciadv.abd9045.

15 S. Hong, F. Ming, Y. Shi, R. Li, I. S. Kim, C. Y. Tang, H. N. Alshareef and P. Wang, *ACS Nano*, 2019, **13**, 8917–8925.

16 L. Ding, D. Xiao, Z. Lu, J. Deng, Y. Wei, J. Caro and H. Wang, *Angew. Chemie - Int. Ed.*, 2020, **59**, 8720–8726.

17 Z. Zhang, S. Yang, P. Zhang, J. Zhang, G. Chen and X. Feng, *Nat. Commun.*, 2019, **10**, 2920.

18 X. Zhu, J. Hao, B. Bao, Y. Zhou, H. Zhang, J. Pang, Z. Jiang and L. Jiang, *Sci. Adv.*, 2018, **4**, 1–9.

19 R. Li, J. Jiang, Q. Liu, Z. Xie and J. Zhai, *Nano Energy*, 2018, **53**, 643–649.

20 J. Gao, W. Guo, D. Feng, H. Wang, D. Zhao and L. Jiang, *J. Am. Chem. Soc.*, 2014, **136**, 12265–12272.

21 Z. Zhang, L. He, C. Zhu, Y. Qian, L. Wen and L. Jiang, *Nat. Commun.*, 2020, **11**, 875.

22 Z. Wu, P. Ji, B. Wang, N. Sheng, M. Zhang, S. Chen and H. Wang, *Nano Energy*, 2021, **80**, 105554.

23 Z. Zhang, P. Zhang, S. Yang, T. Zhang, M. Löffler, H. Shi, M. R. Lohe and X. Feng,

Proc. Natl. Acad. Sci., 2020, **117**, 13959–13966.
24 Z. Wu, T. Zhang, B. Wang, P. Ji, N. Sheng, M. Zhang, Q. Liang, S. Chen and H. Wang, *Nano Energy*, 2021, **88**, 106275.
25 W. Xin, H. Xiao, X. Y. Kong, J. Chen, L. Yang, B. Niu, Y. Qian, Y. Teng, L. Jiang and L. Wen, *ACS Nano*, 2020, **14**, 9701–9710.